Journal of The Electrochemical Society, **157** (8) H847-H852 (2010)
0013-4651/2010/157(8)/H847/6/$28.00 © The Electrochemical Society

Understanding the Growth of β-$FeSi_2$ Films for Photovoltaic Applications: A Study Using Transmission Electron Microscopy

A. S. W. Wong,[a,z] **G. W. Ho,**[b] **and D. Z. Chi**[a]

[a]*Institute of Materials Research and Engineering, Agency for Science, Technology, and Research, Singapore 117602*
[b]*Department of Electrical and Computer Engineering, National University of Singapore, Singapore 117576*

The microstructure of β-$FeSi_2$ films grown on Si using magnetron sputtering has been examined using various electron microscopy techniques. After annealing, the differences in interfacial roughness and grain size with different target materials are investigated using secondary electron and transmission electron microscopy techniques. Here, we study the variation in microstructures with sputtered materials. We observed, for Fe sputtered onto Si followed by rapid thermal anneal, the formation of nanosized $FeSi_2$ grains (∼120 nm) with a rough surface and film/Si interface. These morphologies and microstructure are very different when $FeSi_2$ is sputtered onto Si and annealed; instead, the formation of micrometer $FeSi_2$ grains (∼1 to 5 μm) with sharp surfaces and interfaces is observed. In addition, the effect of oxygen on the growth of $FeSi_2$ has also been studied. Our results show that oxygen impurities in the films result in the formation of Si_xO_y nanoparticles in the $FeSi_2$ matrix upon anneal.
© 2010 The Electrochemical Society. [DOI: 10.1149/1.3454741] All rights reserved.

Manuscript submitted March 2, 2010; revised manuscript received May 10, 2010. Published July 2, 2010.

β-iron disilicide (β-$FeSi_2$) has a direct bandgap of 0.80–0.85 eV and a high optical adsorption coefficient of 10^5/cm^2 at 1 eV.[1,2] It is present in abundance in the earth's crust, which makes it relatively cheap. Given that Fe and Si are nontoxic, it is also considered to be an environmentally friendly material compared to materials such as copper indium gallium selenide. This host of advantages makes β-$FeSi_2$ a desirable candidate for photovoltaic and light emitting applications.[3-6] Although the theoretical energy conversion efficiency for this material is 16–23%,[7-10] the highest laboratory-based result reported so far is 3.7% at 100 mW/cm^2, which is preceded by 0.35% at 100 mW/cm^2.[11] Liu et al.[11] were able to achieve a significant increase in cell efficiency from 0.35 to 3.7% by fabricating high quality epitaxial β-$FeSi_2$ films through the introduction of a thin β-$FeSi_2$ template layer preformed on Si(111) substrates at 400°C, followed by annealing at 600°C.[12] In addition, the template layer also acts as a blocking layer for Fe diffusion into the Si(111) substrate during the high temperature anneal.[12] Fe introduces defect levels in Si, which can act as traps for photogenerated carriers thereby reducing solar cell efficiency.[13,14]

So far, β-$FeSi_2$ films have been grown using facing target sputtering[12-14] and molecular beam epitaxy.[15-18] β-$FeSi_2$ can also be grown using magnetron sputtering,[19] either by depositing Fe onto Si substrate or by depositing $FeSi_2$ directly onto any substrate, followed by annealing. For $FeSi_2$ films grown on Si substrate, the solid-state reaction between Fe and Si substrate can result in a rough surface and interfaces,[20-22] while the direct sputtering of $FeSi_2$ has the flexibility and advantage of depositing on non-Si substrates such as glass and steel.[23] In this context, we explored the possibility of growing β-$FeSi_2$ films using magnetron sputtering with Fe and $FeSi_2$ targets and assessed parameters such as anneal temperature and oxygen impurities on the quality of the films.

Experimental

Si(100) substrates were dipped in dilute HF (1%) for 5 min to remove native oxides. All samples were grown in a Denton sputtering system equipped with two dc, one radio-frequency sputtering cathode, and a sample rotation stage to ensure that a uniform deposition was used to deposit thin films. Deposition was carried out at room temperature. Fe and $FeSi_2$ targets were mounted onto dc cathodes. Cleaned Si substrates were soaked in deionized water for a few minutes and then blow dried in nitrogen gas. The Si substrates were immediately placed into the sputtering chamber. The chamber was subsequently pumped to a base pressure of 5×10^{-7} Torr. With 25 sccm of Ar, a working pressure of 3×10^{-3} Torr was maintained throughout the deposition process. To study the effect of oxygen impurities on film microstructure, a base pressure of 5×10^{-6} Torr was obtained before sputtering. For all deposition runs, the $FeSi_2$ and Fe targets were presputtered for 10–15 min with the shutter closed to remove any form of oxides and organic contaminants that may be present on the targets. Postdeposition anneal was carried out using a rapid thermal annealing (RTA) system in nitrogen at 500–800°C for 60 s. After annealing, the films were cooled to room temperature over a period of 20 min before the samples can be removed.

The film morphologies were determined using a JEOL JSM 6700 field-emission-scanning electron microscope (SEM) system operating in the secondary electron mode at 5 kV. Transmission electron microscopy (TEM) specimens were prepared using conventional grinding, polishing, and dimpling processes. Electron transparent regions were obtained using a Gatan precision ion polishing system. Ar^+ milling was carried out with top and bottom incident gun angles of 8° at 5 keV followed by 4–5° at 3–3.5 keV to minimize specimen damage. Film thicknesses, film/substrate interfaces, and nanostructures were studied using cross-sectional transmission electron microscopy (XTEM) in a Philips CM300 TEM system equipped with a field-emission electron source operated at 300 kV and an extractor voltage of 3.81 kV. Under multibeam conditions, different g values from the film and substrate were excited at the same time and used to form the dark-field images. The same microscope, equipped with a Gatan imaging filter and camera (1024×1024), was used to collect electron energy loss (EEL) spectra for the quantification of the film composition and analysis of the fine structures that are present in the Si L edges of the various samples. All the EEL spectra were collected in diffraction mode with the smallest camera length. For the quantification, the O K (532 eV), Fe L (708 eV), and Si K (1839 eV) edges were acquired at a 1 eV/pixel dispersion and an acquisition time of 2 s. The zero loss peak was shifted by 600 eV to acquire the O K and Fe L edges and shifted by 1300 eV to acquire the Si K edge. The two separate spectra were then spliced to given continuous EEL spectra with EEL ranging from 500 to 2200 eV. To have a better resolution for the fine structure analysis of the Si L edge, the Si L edges were acquired with a dispersion of 0.2 eV/pixel and a 2 s acquisition time. For elemental quantification using X-rays, the scanning transmission electron microscopy (STEM) energy-dispersive X-ray (EDX) analysis was carried out using an FEI M-STEM system at 80 kV. The accelerating voltage was set at 80 kV to minimize sample damage at high accelerating voltage. For STEM analysis, the system was equipped with an electron probe of 1 nm and an energy-dispersive analysis by X-ray detector that al-

[z] E-mail: wonga@imre.a-star.edu.sg

Downloaded 25 Jul 2010 to 137.132.123.69. Redistribution subject to ECS license or copyright; see http://www.ecsdl.org/terms_use.jsp

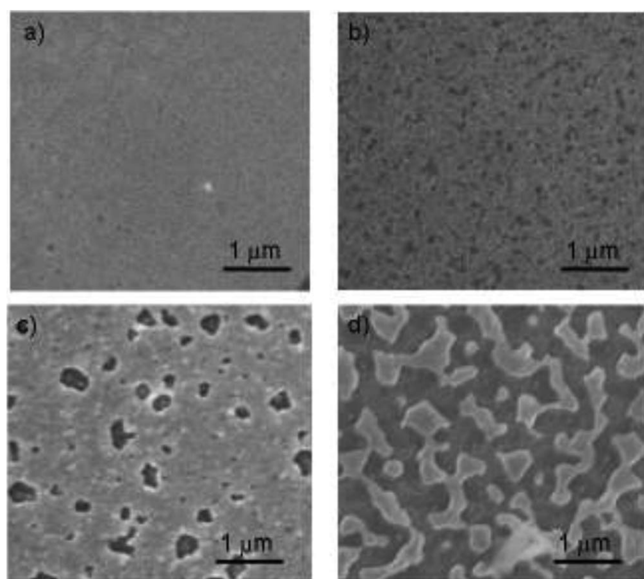

Figure 1. Secondary electron images of Fe/Si films formed by depositing Fe on Si(100) substrate and annealed at (a) 500, (b) 600, (c) 700, and (d) 800°C. Noticeable roughening of film surface and film agglomeration are observed at 600, 700, and 800°C, respectively.

lows elemental quantification of nanometer regions. In addition, high angle annular dark-field imaging (HAADF) using an HAADF detector provided qualitative information on the mean atomic number variation in films as higher atomic number atoms scatter electrons more strongly than lower atomic number atoms. In HAADF, the bright contrast in these images suggests the presence of heavier atoms, assuming that film thickness does not change across the analyzed area. Phase determination was carried out using X-ray diffraction from a general area detector diffraction system operated at 40 kV and 40 mA.

Results and Discussion

Solid-state reaction between Fe and Si(100) substrate.— Figure 1 shows the evolution of the surface morphology of Fe film deposited Si(100) substrates as annealing temperature increases from 500 to 800°C. Before annealing (not presented here), the Fe film surface displays a very flat and featureless morphology. Following a short anneal (in N_2 for 60 s), surface roughening after a 500°C anneal and onset of agglomeration is observed at 600°C (Fig. 1b). This becomes more severe at 700 and 800°C. At 800°C, complete film separation into islands is observed (Fig. 1d). Most island sizes vary between 1 and 2 μm. In addition, 200 nm islands are also observed (Fig. 1d).

XTEM was able to uncover more information on the structural evolution during silicidation. Figure 2a-d shows XTEM images of the sample annealed at 500–800°C. Two distinct layers are observed at 500–700°C, while islands are observed above a single layer at 800°C. The STEM EDX analyses of the layers show that the top layer consists of unreacted Fe and the bottom layer consists of FeSi (500 and 600°C) and $FeSi_2$ (700–800°C). The films are rough at both the film surface and film/substrate interface at all temperatures. Grain boundaries (Fig. 3a), identified by the presence of grooves at the $FeSi_2$/substrate interface and even the $FeSi_2$ surface, are clearly visible. In all the samples, each grain is a perfect single crystal (Fig. 3), with no noticeable line defects such as stacking faults or dislocations. The high resolution transmission electron microscopy (HRTEM) image also clearly shows the presence of $FeSi_2$(402) and $FeSi_2$(400) lattice fringes (Fig. 3b and c). The average grain size, measured between vertical grain boundaries, is ~120 nm.

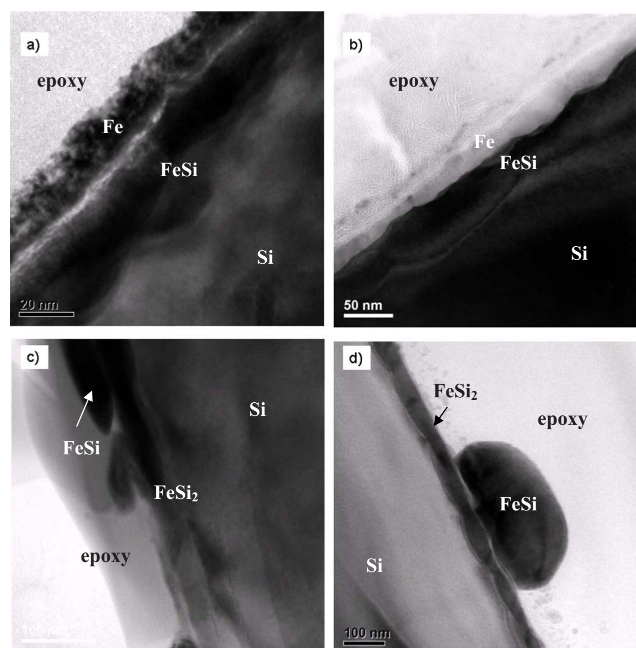

Figure 2. (Color online) Bright-field TEM image of Fe/Si films formed by depositing Fe on Si(100) substrate and annealed at (a) 500, (b) 600, (c) 700, and (d) 800°C. STEM EDX analysis reveals the top layers in (a)-(d) to be unreacted Fe and bottom layers in (a) and (b) to be FeSi while the bottom layers in (c) and (d) to be $FeSi_2$. (d) The grain boundary grooves and estimated grain size of ~120 nm.

The deposition of Fe onto Si(100) and the subsequent annealing result in a solid-state reaction between Fe and Si, where Fe and Si diffuse and react to form iron disilicide. With an unlimited supply of Si atoms from the Si substrate, the final iron silicide phase is largely dependent on the anneal temperature.[24,25] In many metal–silicide systems, for example, the Ni–Si system, a solid-state reaction between Ni and Si can result in the sequential formation of Ni_2Si, NiSi, and $NiSi_2$. $NiSi_2$ is a high temperature Si-rich phase, which forms only at an annealing temperature ≥700°C.

In the Fe–Si system, for annealing at <700°C, the reaction pathway in Eq. 1 is likely the case

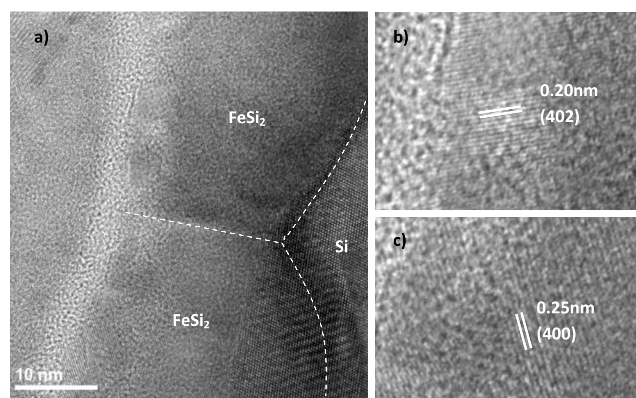

Figure 3. (a) HRTEM image taken from Fe/Si film annealed at 800°C. It shows the surface, interface, and grain boundary between two grains, which are clearly marked by white dotted lines. The dark contrast toward the bottom right of the image is likely due to moiré fringes caused by overlapping Si and β-$FeSi_2$ crystals. Also note the larger groove angle at the $FeSi_2$/Si interface compared to the surface. (b) and (c) (402) and (400) lattice fringes observed within the $FeSi_2$ grains, respectively.

Downloaded 25 Jul 2010 to 137.132.123.69. Redistribution subject to ECS license or copyright; see http://www.ecsdl.org/terms_use.jsp

$$\text{Fe} + \text{Si} \rightarrow \text{FeSi} \qquad [1]$$

At an annealing temperature ≥700°C, the solid-state reaction results in the consumption of more Si. It is highly possible that FeSi formed at a lower temperature but transformed to $FeSi_2$ at higher temperatures, as illustrated below

$$\text{FeSi} + \text{Si} \rightarrow \text{FeSi}_2 \geq 700°\text{C} \qquad [2]$$

In addition, the high temperature anneal results in the formation of grooves at grain boundaries,[20] as observed in Fig. 3. This phenomenon occurs owing to the equilibrium at the groove root and surface diffusion away from the high curvature region formed, which is applicable to the groove roots at the film/substrate interface. The surface and interface roughness largely depends on the energy balances at the upper and lower grain boundary grooves. When the critical grain size is reached, film agglomeration can occur. This is observed in the unreacted Fe films annealed at 800°C. This is like the Ni–Si system, where NiSi remains relatively continuous due to kinetic mass transport limitations while film agglomeration at 700°C is driven by the lower surface energy of the Si(100) substrate.[21,22] The large groove's angle at the interface compared to the surface can be attributed to the larger surface energy with respect to interfacial energy.[20]

Liu et al.[26] reported the effect of stoichiometry on the $FeSi_2$/Si(111) interfacial roughness. Using Auger electron spectroscopy depth profiling, the most abrupt interface is observed for the Si/Fe ratio of 2.6 as compared to 2.0 and 1.0. XTEM images taken at the interface regions show large grains and grain boundaries vertical to the β-$FeSi_2$/Si interface for Si/Fe = 1.0. Using XTEM, the surface and interface are observed to be undulated. Although it was not specifically highlighted, the grain size, determined from the difference in diffraction contrast of each grain, is not more than 300 nm. In contrast, the film with a deposition ratio of Si/Fe = 2.0 shows a relatively homogeneous structure containing few grains, uniform film thickness, and a flat interface. For the Si-rich film with Si/Fe = 2.6, XTEM images show lamellar structures with parallel separated layers, where each layer contains a large number of small grains, some smaller than 100 nm. In this case, the β-$FeSi_2$ film has uniform thickness and sharp interfaces.

Although no clear attribution was given on the effect of film stoichiometry on surface and interface roughness, for the nonstoichiometric film (Fe/Si = 1.0), the excess Si required for $FeSi_2$ formation has to be provided by the Si substrate. This is similar to the solid-state reaction in our films, where Fe reacts with the Si substrate during the high temperature anneal. However, the extent of interfacial roughening may be greater in our films due to the greater extent of Fe and Si diffusion at high temperature. However, Fe deposited onto Si(111) at 400°C and subsequently annealed at 600°C to form epitaxial β-$FeSi_2$ has a sharp interface even though Si from the substrate was consumed to form the β-$FeSi_2$ template.[11]

Solid-state reaction of $FeSi_2$/Si(100).— Here, we study the microstructure, surface, and interfacial roughness of the films prepared with $FeSi_2$ targets. Our study shows that β-$FeSi_2$ begins to form at 600°C. Figure 4 shows the X-ray diffraction patterns of the various samples after annealing, which confirms the formation of β-$FeSi_2$ at 600–800°C.

Figure 5a-d shows the XTEM image of an $FeSi_2$ film formed by sputtering for 30 min onto the Si(111) substrate at room temperature. This is followed by postdeposition annealing at 600–800°C for 60 s. The surface and interface in these films are extremely flat. An extensive XTEM study of at least 10 samples reveals the presence of a few vertical grain boundaries, which suggests that these films consist of very large grains, making the grain boundaries difficult to detect over the limited thin region of a TEM specimen. Traditionally, grain size can be determined easily using plan-view SEM or TEM. In the former, grain grooves enhance the visibility of the grain boundaries. As these β-$FeSi_2$ films remain flat with no visible grain boundary grooves even after a 60 s RTA at 800°C, it is impossible to determine the grain size using plan-view SEM analysis. Furnace annealing at 800°C for 3 h, however, enhances grain boundary grooving, thus revealing the grain boundaries, making the grains easily identifiable using plan-view SEM analysis (Fig. 6a). Figure 6b is a typical plan-view TEM image of a sample annealed at 600°C for 60 s. A detailed study of several samples annealed at various temperatures using plan-view TEM and SEM shows slight changes in the grain size in the annealing temperature range of 600–800°C. Even after many hours of annealing (up to 3 h) in the furnace, a grain size varying between 1–5 μm is observed.

As already discussed in the Introduction, for films with a Si/Fe ratio ≥2, the film/substrate interface remains flat. This is likely the case for the films sputtered from $FeSi_2$, which explains the sharp interface observed in these films. In addition, the large grain size in these films also suggests a smaller nucleation site density, as compared to the silicidation of Fe/Si, which has an average grain size of ~120 nm. This is also strikingly different from that reported by Liu

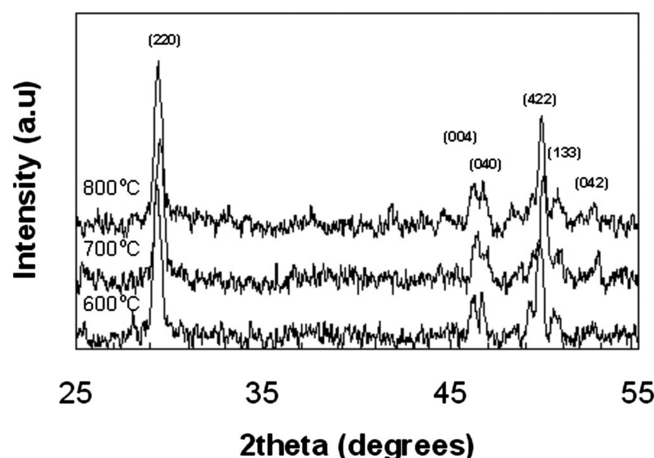

Figure 4. X-ray diffraction patterns of Fe/Si(100) films annealed at 600–800°C. The indexed peaks are those of β-$FeSi_2$.

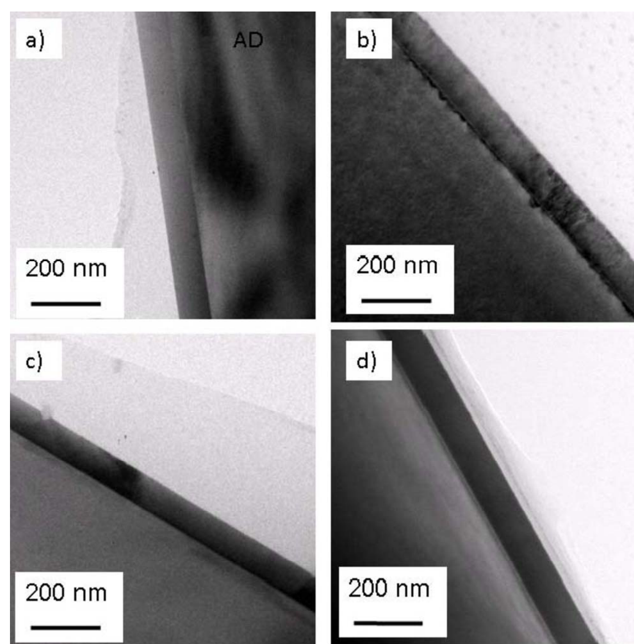

Figure 5. (Color online) Bright-field TEM images of $FeSi_2$/Si films annealed at (a) 500, (b) 600, (c) 700, and (d) 800°C. Note the extremely flat surfaces and film/substrate interfaces in all samples.

Downloaded 25 Jul 2010 to 137.132.123.69. Redistribution subject to ECS license or copyright; see http://www.ecsdl.org/terms_use.jsp

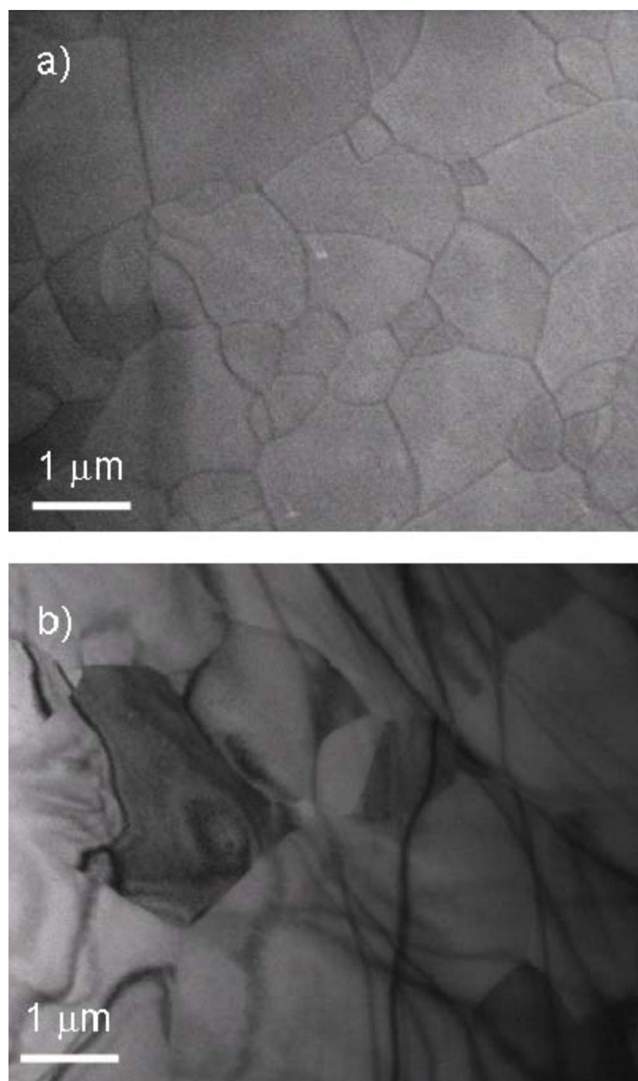

Figure 6. (Color online) Secondary electron image of a $FeSi_2$/Si sample annealed at 850°C for 3 h. Grain boundary grooving arises due to extended annealing time, which reveals grain boundaries. (b) Plan-view TEM image (taken under multibeam condition) of a $FeSi_2$/Si sample annealed at 600°C for 60 s. Note the grain size similar to that observed in (a) despite the lower annealing temperature and time.

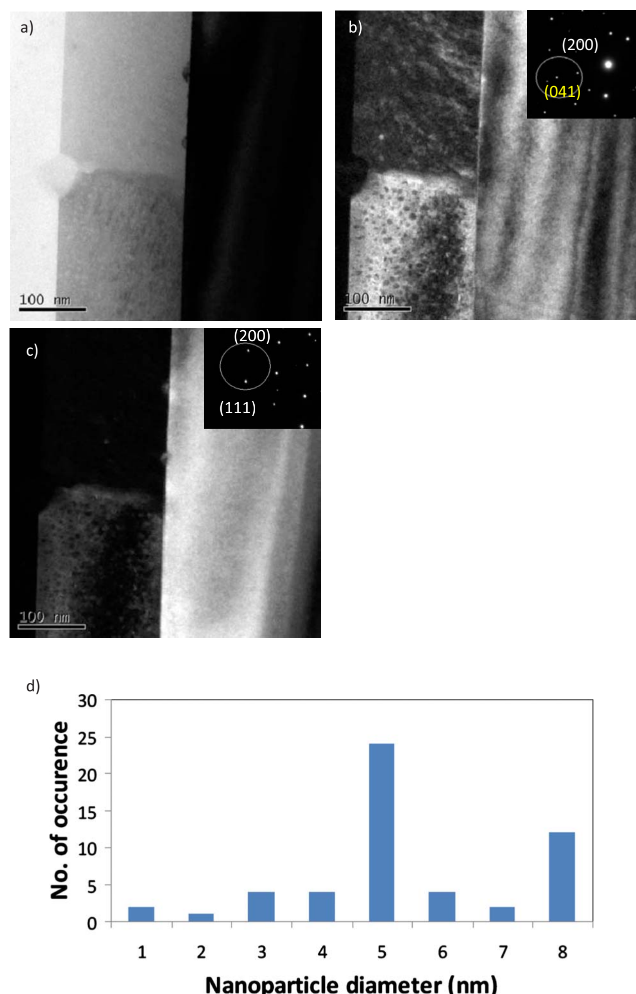

Figure 7. (Color online) TEM images of oxygen-rich $FeSi_2$ films annealed at 750°C for 60 s. (a) Bright-field TEM image obtained at edge-on condition. (b) and (c) Dark-field TEM images obtained using different *g* values. Insets show the corresponding diffraction patterns, and the circle highlights the spots that are used to form the multibeam dark-field images and not the exact size of the objective aperture used. White labels indicate the Si spots while the yellow label indicates the $FeSi_2$ spot. (d) Size distribution of the nanoparticles.

et al.,[26] with an average grain size <1 μm. In addition, it is also plausible that Fe and Si diffuse across shorter distances during silicidation, compared to the Fe/Si case, which may be partly the reason for the lower $FeSi_2$ formation temperature as compared to Fe/Si (700°C). Lastly, the larger grains observed are possibly due to a more efficient coalescence and growth of the grains.[27]

Effect of oxygen impurities in $FeSi_2$/Si(100).— Next we attempt to study the effect of oxygen impurities on the microstructure of the iron silicide films. Figure 7 is a series of bright-field and dark-field TEM images of a $FeSi_2$/Si(100) film grown with a base pressure of 5×10^{-6} Torr and after annealing at 750°C for 60 s. Two distinct $FeSi_2$ grains bordered by a vertical grain boundary are observed (Fig. 7a). In the same image, nanoparticles are also observed within the films. Multibeam dark-field conditions were used to form the dark-field images. g(041) for the film and g(200) for the Si substrate were used to form Fig. 7b, which shows the substrate and $FeSi_2$ matrix to be strongly diffracting. Figure 7c is also taken under the multibeam condition, where only the Si spots, g(200) and g(111), are strongly diffracting. Using a combination of bright-field and dark-field TEM images, we are able to obtain the particle size distribution within the film (Fig. 7e). Most of the nanoparticles are ~ 5 nm in diameter.

Figure 8a is an HAADF image of the same region. The particles are darker in contrast compared to the $FeSi_2$ matrix. As an HAADF image is atomic number sensitive, we are able to conclude that the nanoparticles have a smaller average atomic number compared to the matrix. The EDX line profile (Fig. 8b) performed with a step size of 1 nm across one nanoparticle confirms the nanoparticle to be Fe-poor compared to the surrounding matrix. In the matrix, the ratio of the elements in atom % in Fe:Si:O is 22:66:12 but is 14:75:11 within the nanoparticle. As the nanoparticle and the surrounding $FeSi_2$ matrix encapsulating the nanoparticle are Si-containing, Fe is still observed at the center of the silicon oxide nanoparticle. It is impossible to determine the exact composition of the nanoparticle because TEM EDX is done in projection of the sample thickness.

Figure 9 is a series of EEL spectra and Si L edges taken from various samples. Figure 9a and b is acquired from the films grown at 5×10^{-6} and 5×10^{-7} Torr, respectively. Figure 9c is acquired from the 100 nm amorphous SiO_2 grown on Si. The O:Fe:Si determined from the quantification of the EEL spectra (in atom %) for the

Downloaded 25 Jul 2010 to 137.132.123.69. Redistribution subject to ECS license or copyright; see http://www.ecsdl.org/terms_use.jsp

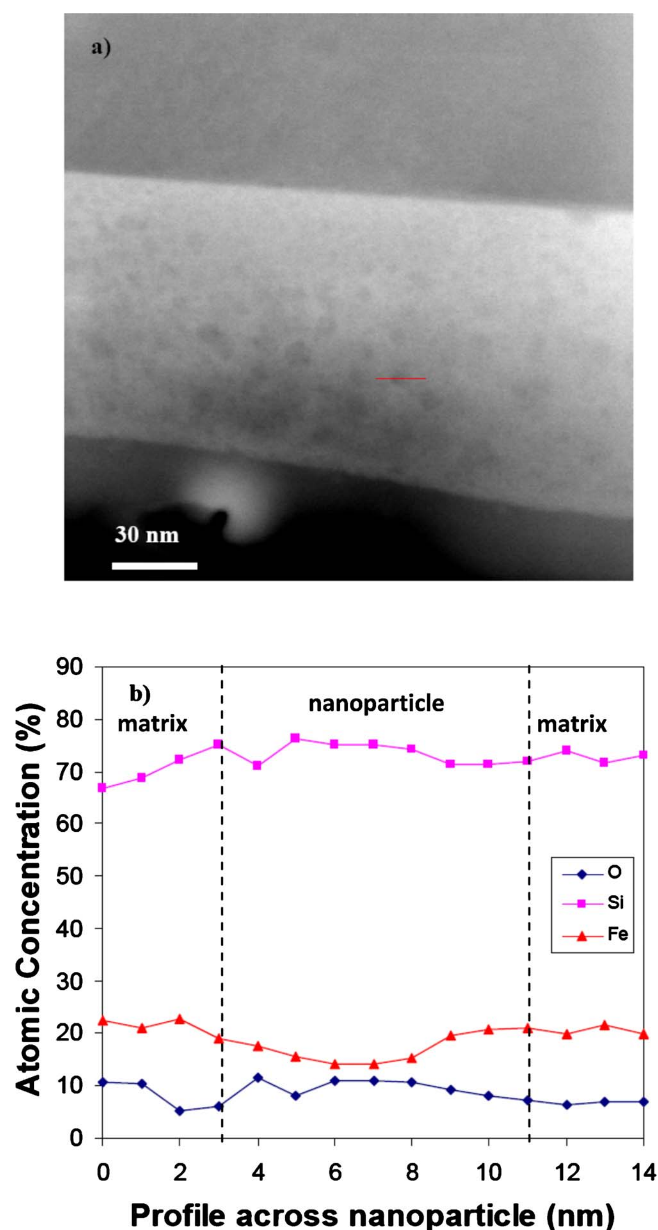

Figure 8. (Color online) (a) HAADF image of the oxygen-rich $FeSi_2$ films annealed at 750°C for 60 s. (b) EDX line profile of O, Fe, and Si in atom % across a nanoparticle. The dotted lines indicate the boundary between the nanoparticle/matrix interface.

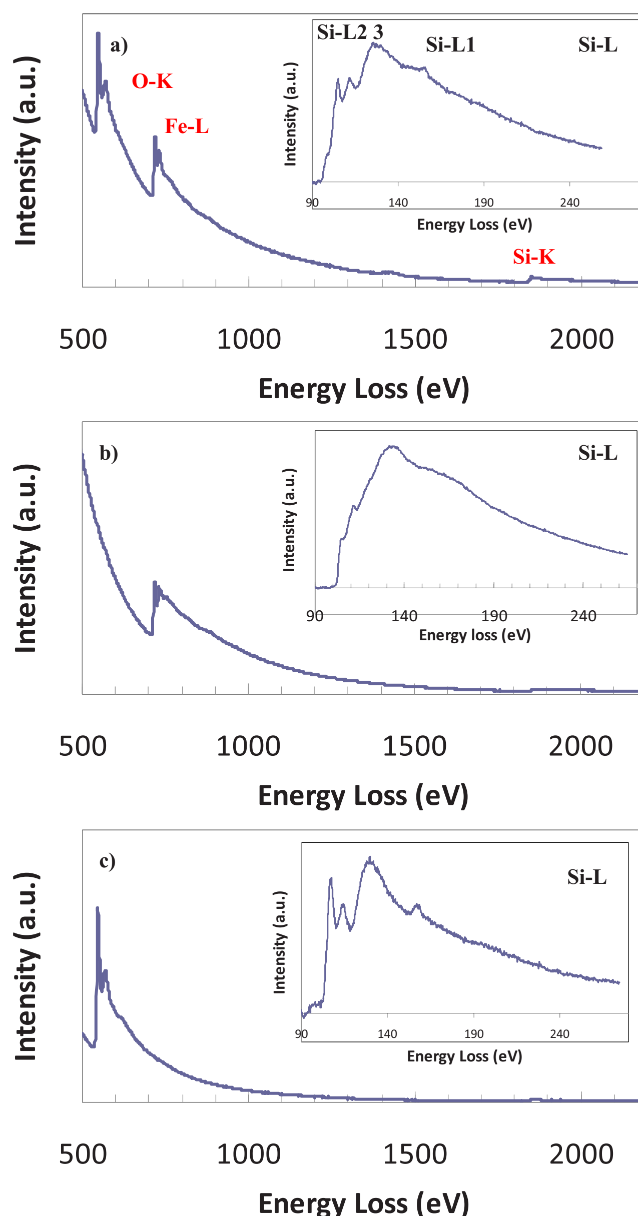

Figure 9. (Color online) EEL spectra showing the O, Fe, and Si edges for (a) oxygen-rich $FeSi_2$ film, (b) oxygen-free $FeSi_2$ film, and (c) SiO_2 film. The inset is the higher resolution EEL spectra showing the Si L edges (from 90 to 300 eV).

oxygen-rich, oxygen-free, and SiO_2 films are 31:15:56, 0:30:70, and 55:0:45, respectively. From this quantification, we can conclude that the oxygen-free films should be $FeSi_{2+x}$. In addition, we can clearly see the difference in fine structure between the three Si L edges (see inset). The film with O has L2 and L3 edges that are very similar to the SiO_2 film compared to the pure film. The EDX and EEL spectra confirm that silicon oxide nanoparticles are formed in the oxygen-rich $FeSi_2$ films.

The mechanism of producing silicon oxide nanoparticles by sputtering and annealing may have involved a few processes. The first is the incorporation of oxygen into the $FeSi_2$ films. In magnetron sputtering, a low base pressure ($<5 \times 10^{-7}$ Torr) is usually required to prevent the formation of native oxides on the Si substrates and incorporation of oxygen into the films. A high base pressure results in a higher level of oxygen impurities in the film growth. Upon annealing, the species within the film diffuse and react. In this case, oxygen within the film can potentially react with Si and Fe that are present in the film. We examine the reaction in terms of thermodynamics and kinetics. From the thermodynamics perspective, the formation of the Si_xO_y oxide nanoparticles can also possibly be driven by a reduction in the free energy of the whole system. In addition, the reaction products are also possibly kinetically controlled, given the very high temperature but short anneal time used in these experiments. Although the amount of oxygen in the film is high, it may be insufficient to form a uniform layer of oxide. Instead, we observed discrete oxide nanoparticles ($\sim$7 nm) within the $FeSi_2$ matrix. The presence of excess Si in the film can also promote the formation of Si_xO_y nanoparticles. The STEM EDX analysis, together with the XTEM images of the $FeSi_2$/Si(100) films annealed at various temperatures showing sharp film/Si interfaces and composition study using EEL, allowed us to conclude that the films contain excess Si and are nonstoichiometric ($FeSi_{2+x}$).

Downloaded 25 Jul 2010 to 137.132.123.69. Redistribution subject to ECS license or copyright; see http://www.ecsdl.org/terms_use.jsp

Conclusion

Various TEM techniques were employed to characterize the growth of $FeSi_2$ films using magnetron sputtering and annealing. For pure Fe sputtered onto Si substrates, the solid-state reaction between Fe and Si yields nanosized β-$FeSi_2$ grains with rough surfaces and interfaces. This is due to the high nucleation site density and large surface and interfacial energies. By sputtering $FeSi_2$ directly onto Si and annealing, micrometer β-$FeSi_2$ grains with a sharp film/Si interface can be obtained due to the lower nucleation site density during growth. Lastly, the presence of oxygen impurities, excess Si in the films, and the driving force to lower energy in the whole system are likely the reasons for favoring the formation of silicon oxide nanoparticles embedded within the $FeSi_2$ matrix.

Acknowledgment

The authors acknowledge Joyce Tan Pei Ying of the Institute of Materials Research and Engineering, A*STAR, for her assistance with the STEM EDX measurements on the M-STEM.

Institute of Materials Research and Engineering assisted in meeting the publication costs of this article.

References

1. M. C. Bost and J. E. Mahan, *J. Appl. Phys.*, **58**, 2696 (1985).
2. K. Yamaguchi and K. Mizushima, *Phys. Rev. Lett.*, **86**, 6006 (2001).
3. K. Lefki and P. Muret, *J. Appl. Phys.*, **74**, 1138 (1993).
4. S. N. Wang, N. Otogawa, Y. Fukuzawa, H. L. Shen, H. Tanoue, T. Kojima, Y. Nakayama, and Y. Makita, *Proc. SPIE*, **5065**, 188 (2003).
5. I. Nishida, *Phys. Rev. B*, **7**, 2710 (1973).
6. S. N. Wang, N. Otogawa, Y. Fukuzawa, Y. Suzuki, T. Ootsuka, Z. X. Liu, M. Osamura, T. Mise, Y. Nakayama, H. Tanoue, et al., in *Proceedings of the Third World Conference on Photovoltaic Energy Conversion*, IEEE, pp. 46–49 (2003).
7. R. H. Bube, *Photovoltaic Materials*, p. 3, Imperial College Press, Amsterdam (1998).
8. M. Powalla and K. Herz, *Appl. Surf. Sci.*, **65–66**, 482 (1993).
9. Z. Yang, K. P. Homewood, M. S. Finney, M. A. Harry, and K. J. Reeson, *J. Appl. Phys.*, **78**, 1958 (1995).
10. Y. Makita, *Proceedings of the First NREL Conference*, IEEE, p. 3 (1997).
11. Z. X. Liu, S. N. Wang, N. Otogawa, Y. Suzuki, M. Osamura, Y. Fukuzawa, T. Ootsukaa, Y. Nakayamab, H. Tanoue, and Y. Makita, *Sol. Energy Mater. Sol. Cells*, **90**, 276 (2006).
12. Z. Liu, Y. Suzuki, M. Osamura, T. Ootsuka, T. Mise, R. Kuroda, H. Tanoue, Y. Makita, S. Wang, Y. Fukuzawa, et al., *J. Appl. Phys.*, **95**, 4019 (2004).
13. K. Wünstel and P. Wagner, *Appl. Phys. A: Solids Surf.*, **27**, 207 (1982).
14. T. Isobe, H. Nakashima, and K. Hashimoto, *Jpn. J. Appl. Phys., Part 1*, **28**, 1282 (1989).
15. Y. Makita, *Mater. Sci. Eng. R.*, **16**, 265 (1996).
16. Y. Makita, Y. Nakayama, Y. Fukuzawa, S. N. Wang, N. Otogawa, Z. X. Liu, M. Osamura, T. Ootsuka, T. Mise, and Y. H. Tanoue, *Thin Solid Films*, **461**, 202 (2004).
17. S. N. Wang, N. Otogawa, Y. Fukuzawa, Y. Suzukiki, T. Ootsuka, M. Osamura, T. Mise, Z. X. Liu, H. Tanoue, Y. Nakayama, et al., *Jpn. J. Appl. Phys., Part 1*, **43**, 4A (2004).
18. Y. Ugajin, T. Sunohara, and T. Suemasu, *Thin Solid Films*, **515**, 8136 (2007).
19. S. Terasawa, T. Inoue, and M. Ihara, *Sol. Energy Mater. Sol. Cells*, **93**, 215 (2009).
20. T. P. Nolan, R. Sinclair, and R. Beyers, *J. Appl. Phys.*, **71**, 720 (1992).
21. A. S. W. Wong, D. Z. Chi, M. Loomans, D. Ma, M. Y. Lai, W. C. Tjiu, S. J. Chua, C. W. Lim, and J. E. Greene, *Appl. Phys. Lett.*, **81**, 5138 (2002).
22. D. Ma, D. Z. Chi, M. E. Loomans, W. D. Wang, A. S. W. Wong, and S. J. Chua, *Acta Mater.*, **54**, 4905 (2006).
23. Y. Nakayama, Z. X. Liu, M. Osamura, T. Ootsuka, Y. Fukuzawa, N. Otogawa, H. Abe, and Y. Makita, *Proc. SPIE*, **6197**, 19718 (2006).
24. F. Nemouchi, D. Mangelinck, J. L. Lábár, M. Putero, C. Bergman, and P. Gas, *Microelectron. Eng.*, **83**, 2101 (2006).
25. E. D. Marshall, C. S. Wu, C. S. Pai, D. M. Scott, and S. S. Lau, *Mater. Res. Soc. Symp. Proc.*, **47**, 161 (1985).
26. Z. X. Liu, M. Tanaka, R. Kuroda, M. Osamura, and Y. Makita, *Appl. Phys. Lett.*, **93**, 021907 (2008).
27. J. E. Brady and J. R. Holum, *Chemistry: The Study of Matter and Its Changes*, John Wiley & Sons, New York (1992).

Downloaded 25 Jul 2010 to 137.132.123.69. Redistribution subject to ECS license or copyright; see http://www.ecsdl.org/terms_use.jsp